HIGH-VELOCITY INTERSTELLAR BULLETS IN IRAS 05506+2414: A VERY YOUNG PROTOSTAR

Raghvendra Sahai,[1] Mark Claussen,[2] Carmen Sánchez Contreras,[3] Mark Morris,[4] and Geetanjali Sarkar[5]

ABSTRACT

We have made a serendipitous discovery of an enigmatic outflow source, IRAS 05506+2414 (hereafter IRAS 05506), as part of a multiwavelength survey of pre-planetary nebulae (PPNs). The *HST* optical and near-infrared images show a bright compact central source with a jetlike extension, and a fanlike spray of high-velocity (with radial velocities up to 350 km s^{-1}) elongated knots which appear to emanate from it. These structures are possibly analogous to the near-IR "bullets" seen in the Orion Nebula. Interferometric observations at 2.6 mm show the presence of a continuum source and a high-velocity CO outflow, which is aligned with the optical jet structure. IRAS 05506 is most likely not a PPN. We find extended NH$_3$ (1,1) emission toward IRAS 05506; these data, together with the combined presence of far-IR emission, H$_2$O and OH masers, and CO and CS $J = 2$–1 emission, strongly argue for a dense, dusty star-forming core associated with IRAS 05506. IRAS 05506 is probably an intermediate-mass or massive protostar, and the very short timescale (200 yr) of its outflows indicates that it is very young. If IRAS 05506 is a massive star, then the lack of radio continuum and the late G to early K spectral type we find from our optical spectra imply that in this object we are witnessing the earliest stages of its life, while its temperature is still too low to provide sufficient UV flux for ionization.

Subject headings: ISM: clouds — ISM: individual (IRAS 05506+2414) — radio lines: ISM — stars: formation — stars: mass loss — stars: pre–main-sequence

1. INTRODUCTION

We report the serendipitous discovery of an energetic outflow source from the object IRAS 05506+2414 (hereafter IRAS 05506). IRAS 05506 was observed as part of our multiwavelength survey of pre-planetary nebulae (PPNs; Sahai et al. 2007), which are transition objects between the asymptotic giant branch (AGB) and planetary nebula evolutionary phases in the lives of low- and intermediate-mass (1–8 $M_{\odot}$) stars. These objects were selected from OH maser catalogs using the *IRAS* color criterion, $F_{25}/F_{12} > 1.4$. Subsequent and continuing observation of the resulting catalog of PPN candidates has shown that the catalog contains PPNs almost exclusively, but the object we discuss here is a notable exception.

In this paper we report our *HST* imaging of IRAS 05506 in the optical and near-infrared, which has revealed a morphology unlike that of any known PPN. We also present additional observations of optical, millimeter-wave, and centimeter-wave lines, as well as the radio continuum toward IRAS 05506, and discuss the possible nature of this source. The plan of our paper is as follows: in § 2 we describe our observations, in § 3 we present the results of these observations, in § 4 we derive the physical properties of IRAS 05506 which show that it is most likely not a PPN but a very young protostar, and in § 5 we summarize our main conclusions.

2. OBSERVATIONS

2.1. Optical and Near-Infrared Imaging with HST

IRAS 05506 (also AFGL 5171) was imaged on UT date 2002 October 20 (GO program 9463), by the High Resolution Camera

[1] Jet Propulsion Laboratory, MS 183-900, Caltech, Pasadena, CA 91109.
[2] National Radio Astronomy Observatory, 1003 Lopezville Road, Socorro, NM 87801.
[3] Departamento de Astrofísica Molecular e Infraroja, Instituto de Estructura de la Materia-CSIC, Serrano 121, 28006 Madrid, Spain.
[4] Division of Astronomy and Astrophysics, UCLA, Los Angeles, CA 90095-1547.
[5] Department of Physics, Indian Institute of Technology, Kanpur 208016, India.

(HRC) of the Advanced Camera for Surveys (ACS), which has a plate scale of 0.025″ pixel^{-1}, using the F606W filter ($\lambda = 0.59$ μm, $\Delta\lambda = 0.157$ μm; exposures were 2×400 s) and the F814W filter ($\lambda = 0.81$ μm, $\Delta\lambda = 0.166$ μm; exposures were 2×200 s). All images were obtained with a two-point dither, and the standard STScI/*HST* pipeline calibration has been applied to all data. We also obtained near-infrared images on UT date 2004 March 23 (GO program 9801) with Camera 2 of the Near Infrared Camera and Multi-Object Spectrometer (NICMOS), which has a plate scale of 0.076″ pixel^{-1} (GO program 9801), using the F110W ($\lambda = 1.1$ μm, $\Delta\lambda = 0.38$ μm; total exposure time was 544 s), F160W ($\lambda = 1.6$ μm, $\Delta\lambda = 0.28$ μm; total exposure time was 56 s), and F205W ($\lambda = 2.1$ μm, $\Delta\lambda = 0.43$ μm; total exposure time was 18 s) filters. For ease of comparison, the NICMOS images have been rotated to the same orientation as the HRC ACS images. Numerous field stars present in the images have been used to achieve satisfactory registration between the optical and near-infrared images.

2.2. Optical Spectroscopy

We obtained long-slit spectra of IRAS 05506 on 2004 November 8 with the Echellete Spectrograph and Imager (ESI; Sheinis et al. 2002) on the 10 m W. M. Keck II telescope at Mauna Kea (Hawaii). The detector was an MIT-LL CCD with 2048×4096 pixel^2 of 15 μm. Total wavelength coverage is ~ 3900–10900 Å. The reciprocal dispersion and the pixel angular scale range from 0.16 to 0.30 Å pixel^{-1} and from 0.120″ to 0.168″, respectively, for the 10 echellette orders (15–6) of ESI, which was used in its echelle mode. The velocity dispersion has a nearly constant value of 11.5 km s^{-1} pixel^{-1} in all orders. We used a $0.5″ \times 20″$ slit with its long side aligned along a vector which passes through two of the most prominent emission knots seen toward this source, with an exposure time of 600 s. Further technical details for these observations are described in Sánchez Contreras et al. (2008) and are similar to those described by Sahai et al. (2005).

2.3. *Millimeter-Wave Interferometry*

The OVRO millimeter-wave array,[6] in its low (L) configuration (for which baselines between antennas range from 15 to 115 m), was used to obtain snapshot observations of the CO $J = 1-0$ line and the 2.6 mm continuum toward IRAS 05506 on 2003 March 17 and 24. The units of the digital spectral line correlator were arranged to provide a total bandwidth of 128 MHz ($\sim$333 km s^{-1}) with a channel spacing of 1 MHz (corresponding to $\sim$2.6 km s^{-1}). The 3 mm continuum emission was observed simultaneously using the dual-channel analog continuum correlator, which provided a total bandwidth of 4 GHz (after combining both IF bands). Total integration time on source and calibrators was $\sim$11 hr.

The calibration of the data was performed using the MMA software package.[7] Data were gain calibrated in baseline-based mode using the quasar J0530+135, which was observed at regular time intervals of $\sim$20 minutes before and after our target. The quasars 3C 273 and 3C 84 were used as passband and flux calibrators.

Reconstruction of the maps from the visibilities was done using the Multichannel Image Reconstruction, Image Analysis, and Display (MIRIAD) software. We Fourier-transformed the measured visibilities with robust weighting (which is an optimized compromise between natural and uniform weighting) for CO and natural weighting for the continuum map for S/N optimization. After that, the images obtained were cleaned and maps restored. The (fitted Gaussian) clean beam for our CO (continuum) map has FWHM $= 3.9'' \times 2.9''$ ($4.6'' \times 3.2''$) and is oriented at P.A. $= -23.6°$ ($-15.3°$). The $1\,\sigma$ noise in our CO (continuum) maps, as measured in channels with no signal, is 0.45 (1.1) mJy beam^{-1}. The conversion factor from CO (continuum) surface brightness to temperature units is 8.0 (6.3) K per Jy beam^{-1}.

2.4. *Centimeter Ammonia, Water, and Methanol Maser Lines*

Observations of the H_2O, NH_3, and methanol lines in the K band, i.e., 22–25 GHz, were obtained with the NRAO[8] Green Bank Telescope (GBT) on 2006 February 28 and March 3. A 6×6 raster scan (step size $= 13''$), centered on the J2000.0 position R.A. $= 05^h53^m43.6^s$, decl. $= +24°14'44.5''$, was performed in right ascension and declination four times during these two days. The beam of the telescope was measured during pointing scans to be $32''$, so the raster was Nyquist-sampled over a small region in the sky of slightly more than $\sim$1$'$. A dual-beam receiver was used at 22–25 GHz, and total power measurements were made, relative to an off-source position of R.A. $= 06^h02^m29.96^s$, decl. $= +26°14'44.2''$ (J2000.0). The GBT spectrometer back end was used to record the total-power spectra in four different 50 MHz frequency bands. These four bands were set to Doppler track the 22235.08 H_2O line ($6_{16} \rightarrow 5_{23}$); the average of the NH_3 (1,1) and (2,2) metastable inversion lines at 23,694.50 and 23,722.63 MHz, respectively; the NH_3 (3,3) metastable inversion line at 23,870.1292 MHz; and the three methanol lines at $\sim$24,932.0 MHz ($3_{2,1} \rightarrow 3_{1,2}\,E$, $4_{2,2} \rightarrow 4_{1,3}\,E$, and $2_{2,0} \rightarrow 2_{1,1}\,E$). The 50 MHz bands provided velocity coverage of $\sim$650 km s^{-1}, centered at $V_{LSR} = 0$ km s^{-1}. Each 50 MHz frequency band had 8192 spectral channels, providing a spectral resolution of 6.1 kHz ($\sim$0.08 km s^{-1}). For each raster position, a total integration time of $\sim$16 minutes was obtained, providing an rms antenna temperature of $\sim$25 mK.

The VLA was used to observe the H_2O line on 2005 June 14, in the CnB configuration (beam $= 1.10'' \times 0.70''$ at P.A. $= 55°$), with the correlator configured to provide 127 spectral channels ($\Delta\nu = 48.8$ kHz) across a bandwidth of 6.25 MHz (84 km s^{-1}). Three velocity ranges, centered at $V_{LSR} = -70$, 0, and +70 km s^{-1} (thus covering a total velocity range from -112 to $+112$ km s^{-1}) were searched by time multiplexing the observations. Each velocity setting was observed for about 10 minutes. The data were calibrated and imaged in the standard way using the NRAO's Astronomical Imaging Processing System (AIPS). The rms noise in the image of each spectral channel was $\sim$15 mJy beam^{-1}.

2.5. *Radio Continuum Observations*

We observed the radio continuum at 8.4 GHz (3.6 cm) in IRAS 05506 on 2005 June 11, using the VLA in the CnB configuration. Approximately 13 minutes were spent on source. The data was calibrated in the usual manner, using AIPS. A continuum image was made using the calibrated u-v data; the synthesized beam, using natural weighting, was $5.1'' \times 1.1''$ at a position angle of $56°$. The rms noise in the image was $\sim$50 μJy beam^{-1}, similar to the expected theoretical noise.

We also examined the region around the position of IRAS 05506 in the NRAO VLA Sky Survey (NVSS; Condon et al. 1998). The NVSS observed at a frequency of 1.4 GHz (21 cm), and typically had noise levels in less-confused regions of about 400 μJy beam^{-1}. This was approximately the noise in the field containing the position of IRAS 05506.

3. RESULTS

3.1. *Optical and Near-Infrared Imaging*

The *HST* F606W image (Fig.1a) shows a compact source (Sa), and a fanlike spray of compact nebulous features K1–K9 that are separated from Sa, but appear to emanate radially from it within a range of position angles ($121°$–$155°$). Examination of the most prominent of these knots (K1–K4) shows that each of them is a highly collimated structure. Most of these knots are seen in the other filters used for the *HST* imaging as well. A few more knots (k10–k12), not seen in the optical images, become visible in the F110W and F160W images in the P.A. range $85°$–$121°$ (Fig. 2),[9] at locations closer to Sa, presumably because these are more highly extincted than the K1–K4 knots. Compact knots like k10 can be distinguished from faint stars in the NICMOS images (labeled fs1–fs4 in Fig. 2) because, relative to their surroundings, the knots are brightest in the F110W image (i.e., at the shortest IR wavelength), whereas the stars are brightest in the F205W images (i.e., at the longest IR wavelength). Significant filamentary structures can be seen all around Sa. The most prominent of these lie in the western hemisphere around Sa, and several of these appear to be radially directed away from the latter (dotted arcs in Fig. 2 delineate angular wedges where these structures are most clearly seen). Two isolated compact nebulosities are also seen in this hemisphere, k13 and k14—the latter has an inverted Y shape, and may represent two (or more) adjoining elongated knots. Knot k13 appears to lie on the periphery of an extended faint structure, described below.

A second compact source (Sb), comprising a close stellar pair with a separation of $0.12''$ (Fig. 1b, *inset*), is seen $5.64''$ to the

---

[9] In this figure, we have retained the original orientation of the NICMOS images (which is different from the optical images taken with the ACS) in order to avoid any loss of fidelity which would result from image rotation.
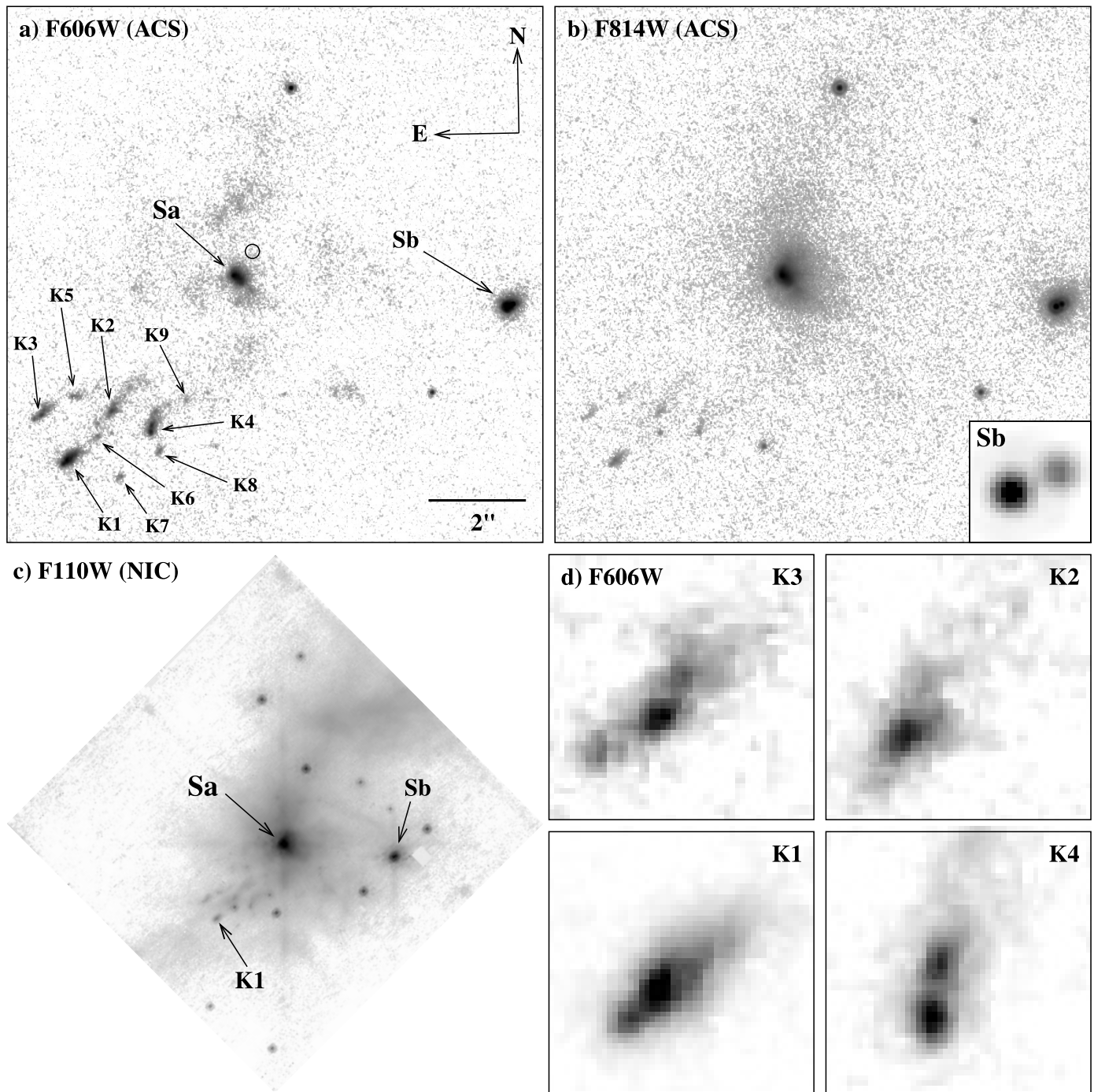
FIG. 1.—*HST* ACS images of IRAS 05506. (*a, b*) Optical images taken with ACS (log stretch). The position (R.A. = $05^h53^m43.54^s$, decl. = $24°14'45.2''$ [J2000.0]) of the H_2O maser emission feature detected with the VLA is shown as a small circle in panel *a*; the size of the circle denotes the positional uncertainty. An expanded view of source Sb (panel *b*, *inset*) shows a close binary pair with a separation of $0.12''$. (*c*) F110W taken with NICMOS (log stretch); a small square patch to the right of Sb corrupted by an instrumental artifact has been blanked out. A few of the features in the panel *a* are also labeled in panel *c* for visual registration. (*d*) Expanded views ($0.63'' \times 0.63''$) of the knots K1–K4 extracted from the F606W image (linear stretch).

west (along P.A. $= -97.6°$) of the main source. Sa has a cometary structure, with a bright peak, Sa-pk, at the northeast end and a jetlike extension, Sa-jet, toward the southwest, along P.A. $\sim 230°$ (Fig.3), which is nearly perpendicular to the average direction of the knot spray seen in the F606W image.

At the location of Sa-pk, the NICMOS F110W (Fig.1*c*), F160W, and F205W (not shown) images show a point source of increasing brightness with wavelength. For this point source, we derive fluxes of 6.5, 54, and 190 Jy, respectively, at 1.1, 1.6 and

2.1 μm from the F110W, F160W, and F205W images, using the photometric calibration information provided by STScI.[10] The 1.1 μm flux is less reliable than the 1.6 and 2.1 μm fluxes because the star is relatively less bright compared to the surrounding nebulosity. The lack of PSF structure toward Sa-pk in the optical images indicates that the central star is not being seen directly at

---

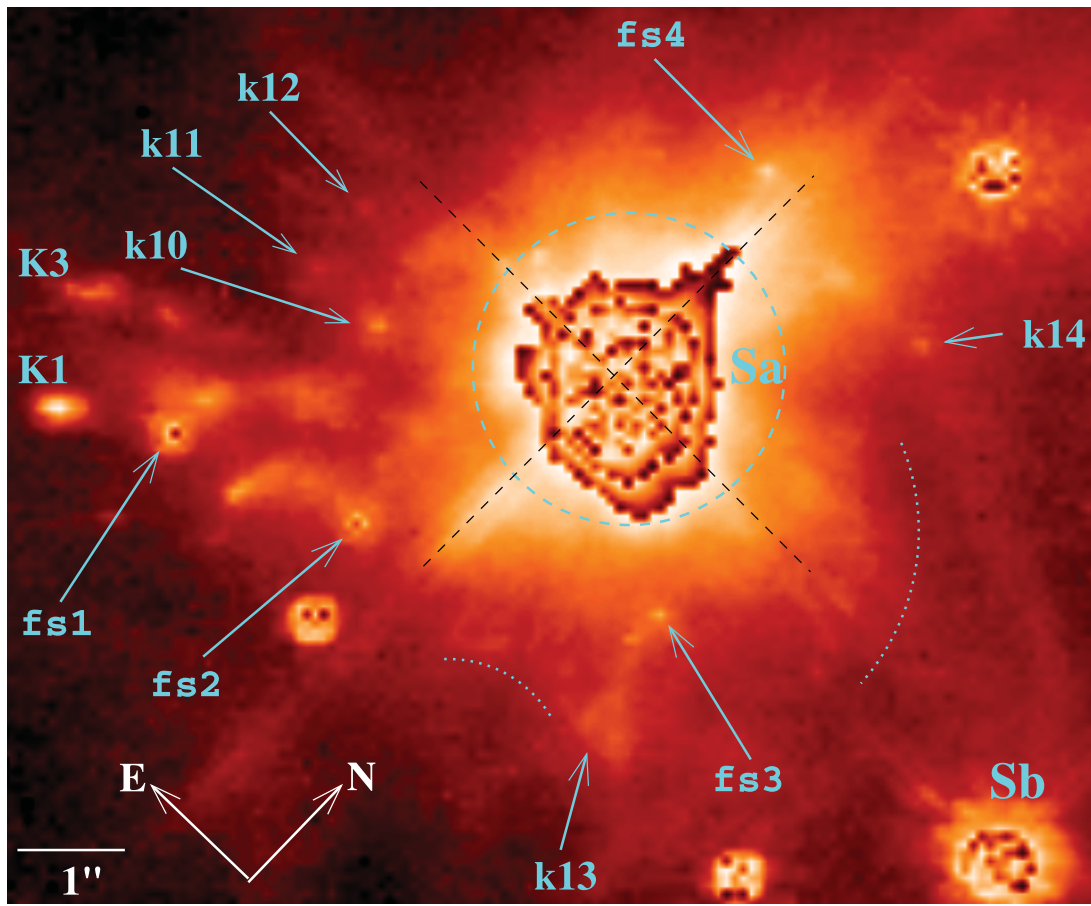[10] Details at http://www.stsci.edu/hst/nicmos/performance/photometry/postncs_keywords.html.

Fig. 2.—F110W NICMOS image of IRAS 05506 highlighting the presence of knotty structures (k10–k14) not seen in the F606W ACS image (some of the common features [K1, K2, Sa, and Sb] are also labeled for visual registration). The gray scale shows log (log I), where I is the intensity; above a threshold value, the color stretch cycles repeatedly through the range of colors utilized, giving the mottled appearance to the brightest regions in the image. Faint stars in this image are labeled fs1–fs4. The dashed circle covers a central region around Sa where knotty structures cannot be reliably distinguished from PSF structures. The dotted arcs delineate angular wedges where faint filamentary structures can be seen; many of these appear to be radially directed away from Sa. The spiky linear structures oriented at $\pm 45°$ to the horizontal (*dashed black lines*) which appear to emanate from Sa are diffraction spikes produced by the telescope optics. Note that the orientation of this image is different from the one in Fig. 1.
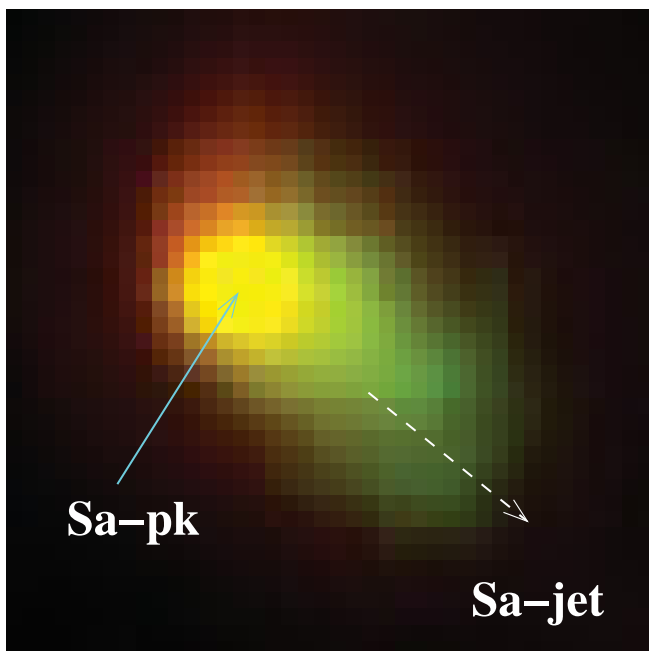

Fig. 3.—*HST* ACS color-composite (*red*: F814W; *green*: F606W) image of feature Sa, shown on a linear stretch. The size of the box is $0.5'' \times 0.5''$. The orientation of this image is the same as in Fig. 1

optical wavelengths. Archival 2MASS images of IRAS 05506 and vicinity (Fig. 4) show that Sa lies atop extended diffuse nebulosity which can be easily seen extending as far as $\sim 20''$–$25''$ toward the northwest.

The position of Sa-pk as measured from the F606W *HST* image is R.A. = $05^h 53^m 43.55^s$, decl. = $24° 14' 44.0''$ (J2000.0). The 2MASS All-Sky Catalog of Point Sources (Cutri et al. 2003) shows only one source (05534356+2414447[11]) within a $\sim 4''$ radius of Sa, and since the uncertainty in the absolute *HST* astrometry is $\lesssim 1''$, the latter represents the near-IR counterpart of Sa. The next nearest 2MASS source is 05534318+2414441, located $\sim 5''$ to the west of Sa, and represents the near-IR counterpart of Sb.

We note the presence of two intriguing features in the vicinity of Sa and Sb, in the F110W and F160W NICMOS images (Fig. 5). One is a tubelike, limb-brightened structure (labeled as "Tube" in the figure) that appears to originate from near Sa and extends toward Sb. The second is a roughly linear structure, L, joining two locally bright regions (B1 and B2); the vector joining these regions passes through Sa. B1 is bright, relatively compact, and appears to be located on the limb brightened periphery of the Tube feature, whereas B2 is much fainter, larger in size, diffuse, and part of an extended nebulosity aligned roughly east-west. In the F205W image, since Sa is much brighter relative to the

[11] The 2MASS source names encode the J2000.0 coordinates of the sources.
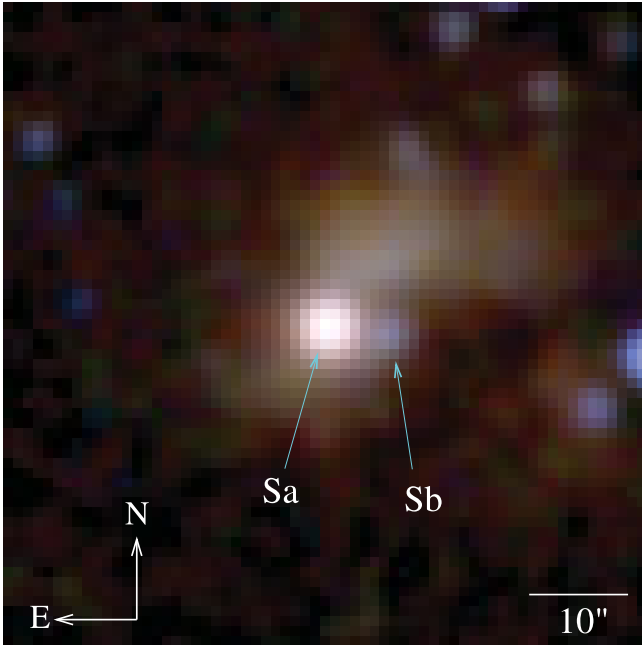
Fig. 4.—Color-composite image made using 2MASS J (*blue*), H (*green*), and K_s (*red*) band images, showing extended nebulosity in the vicinity of IRAS 05506. Each individual image is displayed on a log stretch. Compact sources Sa and Sb are marked for reference.

surrounding nebulosity, only those portions of the Tube and L features which are relatively more distant from Sa can be clearly seen. The similarity of the features in the near-IR images indicates that these are dusty structures seen in scattered ambient starlight. We speculate that the Tube might be a dense-walled cylinder of molecular gas and dust and may represent the wake produced by the motion of Sb through the dense interstellar cloud detected in our NH_3 mapping. The feature L might also be a wake produced by the motion of Sa, or may represent a highly collimated ejection from Sa. Near-infrared emission-line imaging and spectroscopy is needed to better understand the nature of the Tube and L structures.

3.2. Optical Spectroscopy

The slit was aligned along a vector which passes through the knots K1, K2, and Sa. The optical spectra of knots K1 and K2 show high-velocity $H\alpha$ and forbidden line emission such as, e.g., [N II] $\lambda\lambda6548, 6583$, [S II] $\lambda\lambda6716, 6731$, [O I] $\lambda\lambda6300, 6364$, [Ca II] $\lambda\lambda7291.5, 7323.9$, and many lines of [Fe II]. The position-velocity structure and wide velocity widths (~350 km s^{-1}) seen clearly in the strongest of these lines ($H\alpha$, [N II], and [S II]) are characteristic of bow-shock emission (Fig.6) resulting from the interaction of a knotty, high-velocity outflow (or outflows) with dense, ambient material. The knots only show emission lines and no continuum, similar to Herbig-Haro objects. High-velocity emission is also seen at the location of Sa, most likely associated with Sa-jet. In each case we detect blueshifted emission only, which can be interpreted in terms of the near side of a bipolar outflow in which the far (i.e., redshifted) side, if present, is hidden from our view due to local extinction. Unlike the knots, Sa also shows a very red optical continuum.

An analysis of the spectrum (Sańchez Contreras et al. 2008) reveals numerous metallic absorption lines due to Ti I, Fe I, and Ca II in the ~8400–8800 Å wavelength region where the continuum from the central star is less extincted and thus detected with much higher signal-to-noise ratio than at shorter wavelengths. In particular, the Ca II triplet (8498, 8542, and 8662 Å) is quite

strong. The Paschen lines, in the same window, are noticeably absent—Sańchez Contreras et al. (2008) conclude that the most likely spectral type of the star is consistent with late G to early K.

Long-slit optical spectroscopy of IRAS 05506 was reported by Manchado et al. (1990) with a 1.5″ wide slit oriented along P.A. = 80°; they found an emission-line spectrum from an eastern lobe, but only continuum from a western lobe, the lobes being separated by 5″. Our *HST* images show that, if the east lobe is source Sa in that study, as is likely, then the west lobe is source Sb.

3.3. Millimeter-Wave Interferometry

The CO line profile is centered at $V_{LSR} = 7.6$ km s^{-1}, and has a core with a width (FWHM) of ~15 km s^{-1} and weak, broad wings which extend at >50 km s^{-1} on either side of the line center (Fig. 7). The core emission is compact ($\lesssim5''$ in size; Fig. 8). A 5 ± 1 mJy continuum source (at $\lambda = 2.6$ mm) with an unresolved core and a marginal extension along P.A. $\sim 230°$, consistent with the P.A. of the optical jet feature, Sa-jet, is also seen at the same location. A plot of the emission in the extreme red ($V_{LSR} = 49.4$ to 119.6 km s^{-1}) and blue ($V_{LSR} = -36.4$ to -106.6 km s^{-1}) wings (Fig. 8) shows that the outflow is directed roughly along the same P.A. as Sa-jet and the possible extension in the continuum source. This high-velocity bipolar outflow is thus directed along an axis roughly orthogonal to the average direction of high-velocity ejections represented by the optical knot spray (§ 3.2).

3.4. Ammonia, Water, Methanol, and Radio Continuum Observations

With the VLA, we detected a single, spatially unresolved H_2O emission feature (across three spectral channels) at R.A. = $05^h53^m43.54^s$, decl. = $24°14'45.2''$ (J2000.0), at an LSR velocity of 5.9 km s^{-1} and with a peak flux density of 145 mJy beam^{-1} (Fig. 1a, *small circle*). The 1 σ error in the H_2O maser position is $\lesssim0.1''$. Given the astrometric accuracy of the 2MASS catalog ($\lesssim0.1''$), we conclude that there is a small, but significant separation between the locations of the H_2O maser peak and Sa of $0.57''$. This small separation, and the similarity in the H_2O maser radial velocity and the systemic velocity strongly suggests that latter is associated with Sa.

With the GBT, we detected emission in the H_2O and the NH_3 (1,1) and (2,2) lines. In H_2O, two velocity features are detected; one at 6.16 km s^{-1} and another at $V_{LSR} = 11.15$ km s^{-1} (Fig. 9). The FWHM widths of these features, derived from Gaussian fits, are 0.51 ± 0.04 and 0.56 ± 0.01 km s^{-1}. Both velocity features are spatially unresolved. These, as well as the NH_3 (1,1) brightness distribution, peak at the same raster position, which lies $\sim8.4''$ northwest of the VLA H_2O maser position. But given the pointing uncertainties of the GBT and its large beamwidth, this offset is not significant. The H_2O 6.16 km s^{-1} feature is most likely the same as that detected with the VLA (we hereafter call it the 6 km s^{-1} feature). The integrated fluxes of the H_2O maser features for the two epochs, 2005 June 14 and 2006 February 28, are as follows: 0.163 ± 0.017 and 1.03 ± 0.056 Jy km s^{-1} for the 6 km s^{-1} feature and <0.051 (3 σ) and 12.25 ± 0.075 Jy km s^{-1} for the 11 km s^{-1} feature. Thus, over the 1.3 yr period between the two epochs, both features increased dramatically in strength (the 11 km s^{-1} feature by a much larger factor), indicating that they are physically associated and/or the variations represent a common response to the same stimulus (e.g., passage of a shock wave).

The NH_3 lines are surprisingly narrow: the FWHM of the higher signal-to-noise ratio (1,1) line is 0.96 km s^{-1} (discussed further in § 5). The NH_3 emission line profile in the main hyperfine
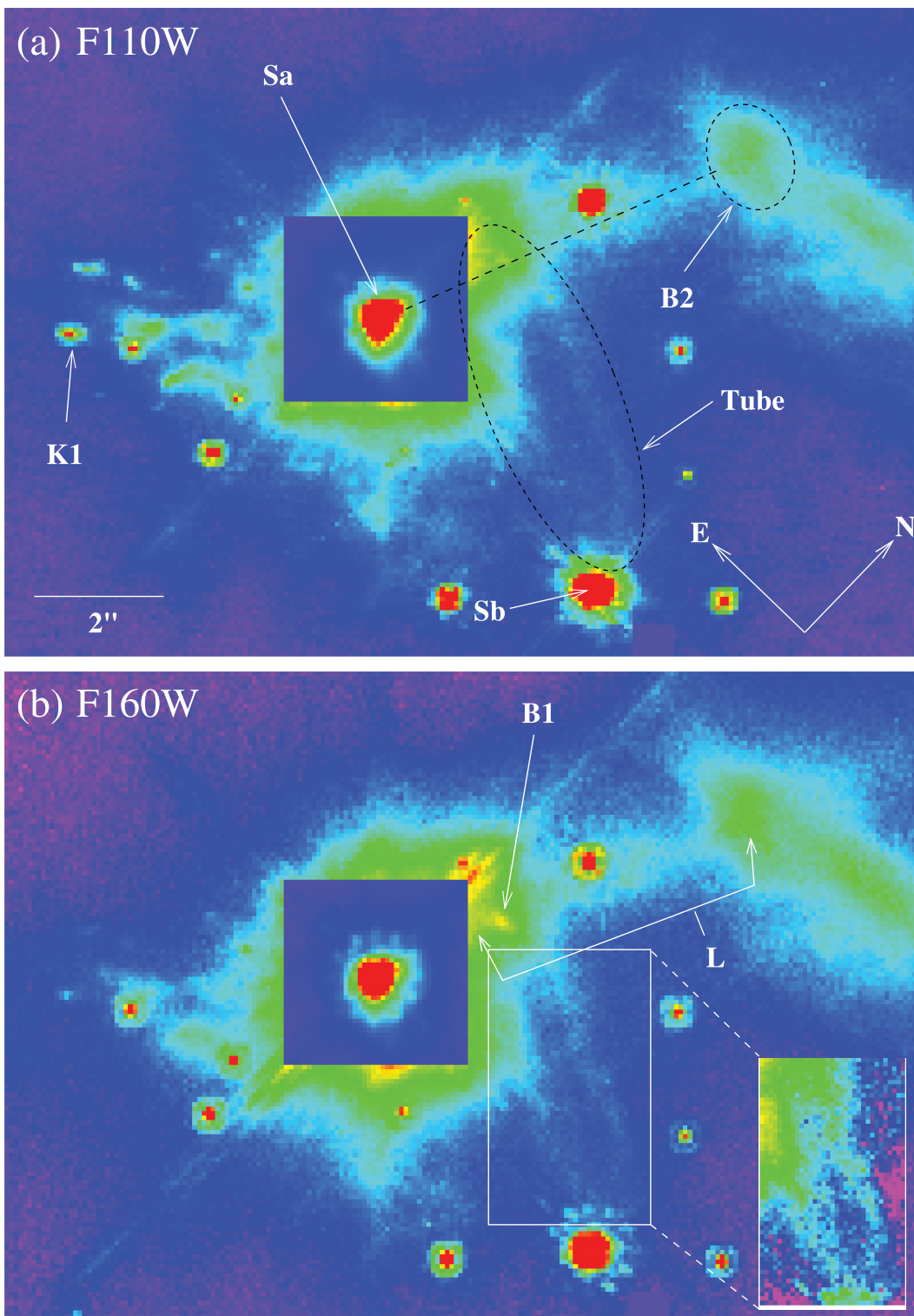
Fig. 5.—(a) F110W and (b) F160W NICMOS images of IRAS 05506 (shown with a square-root stretch and false-color intensity scale) highlighting the presence of low-contrast features. The intensity in the very bright central region surrounding Sa has been scaled down by a factor of 0.06 (0.03) in the F110W (F160W) image in order to better show the structure of the surrounding faint nebulosity. The large ellipse in panel a encircles a tubelike structure (marked as "Tube"); the inset in panel b (*lower right corner*) covers a $2.5'' \times 4.3''$ patch around the Tube with a different stretch to show its faint parts more prominently (the inset shows $I^{0.25}$, where I is the intensity). The dashed straight line in panel a marks a roughly linear structure, L, joining two locally bright regions (B1 and B2). The small ellipse in panel a shows the location of B2, which is more diffuse and extended compared to B1. The spiky linear structures oriented at $\pm 45°$ to the horizontal which appear to emanate from Sa, including the three bright yellow/orange streaks seen to the east of B1, are diffraction spikes produced by the telescope optics. Note that the orientation of these images is different from the one in Fig. 1.
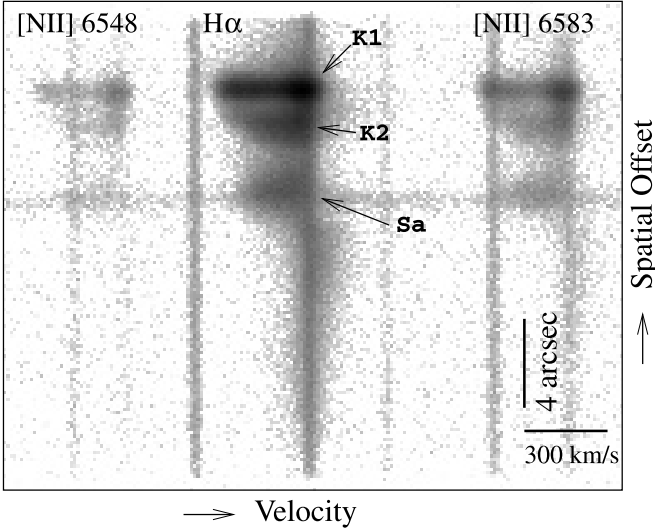
FIG. 6.—Keck ESI long-slit spectra of IRAS 05506 showing high-velocity outflows and bow-shock structures in the Hα and [N II] lines. The narrow vertical features are due to night-sky emission lines.

FIG. 8.—OVRO CO $J = 1-0$ (*contours*) and 2.6 mm continuum (*gray scale*) map of IRAS 05506 (Sa). The clean beam for the CO (continuum) map has a FWHM of $3.9'' \times 2.9''$, P.A. $= -24°$ ($4.6'' \times 3.2''$, P.A. $= -15°$). The yellow, red, and cyan contours show the CO intensity integrated over the V_{lsr} velocity ranges [2.6, 10.4], [49.4, 119.6], and [−36.4, −106.6] km s^{-1}, respectively. The corresponding values of the peak contour intensity (and spacing) are 6.3 (0.66), 3.8 (0.65), and 4.8 (0.65) Jy beam^{-1} (km s^{-1}).

component is centered at $V_{LSR} = 6.21$ km s^{-1} (Fig. 10). The NH$_3$ emission is extended toward the east and northwest; the region of emission is likely slightly larger than $1'$ (the raster was not large enough to measure the full extent of the ammonia emission). We detect weak ammonia (2,2) emission (only in the main hyperfine component, and after smoothing the spectrum by a factor of 4) at the position of the peak of the (1,1) emission. No methanol lines were detected.

Our 8 GHz continuum observations show no continuum emission (3 σ upper limit of 150 μJy) within a field of approximately $40''$ diameter centered on the position of IRAS 05506. From the 1.4 GHz NVSS all-sky survey data, we obtain an upper limit of 1200 μJy.

4. PHYSICAL PROPERTIES OF IRAS 05506

The steep increase in Sa-pk's flux from 0.6 to 2μm strongly indicates that it is a highly extincted stellar source which most likely is driving the energetic outflow responsible for the whole spray of knots. Consistent with this interpretation, we find a bright source in the *Midcourse Space Experiment* (*MSX*: Egan et al. 1999) catalog located at the position of Sa-pk, i.e., at
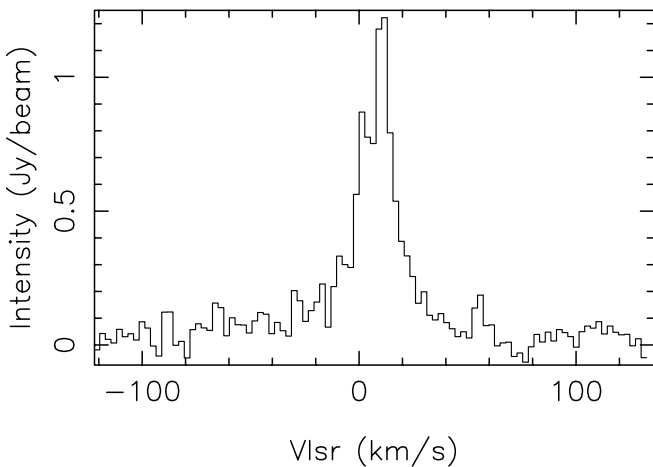
R.A. $= 05^h53^m43.55^s$, decl. $= 24°14'44.0''$ (J2000.0). In this section we derive the physical properties of the central source and its environment, many of which depend on the distance to the source. We estimate a formal kinematic distance of 2.8 kpc to IRAS 05506, using the formulation given by Goodrich (1991). We have taken the average of the source radial velocities from our ammonia and CO data, i.e., 6.9 km s^{-1} as the systemic velocity, and assumed Galactic parameters $R_0 = 8$ kpc, $\Theta = 220$ km s^{-1},

FIG. 7.—Average intensity spectrum extracted from a $3'' \times 3''$ box centered on the peak intensity position in the OVRO CO $J = 1-0$ map.

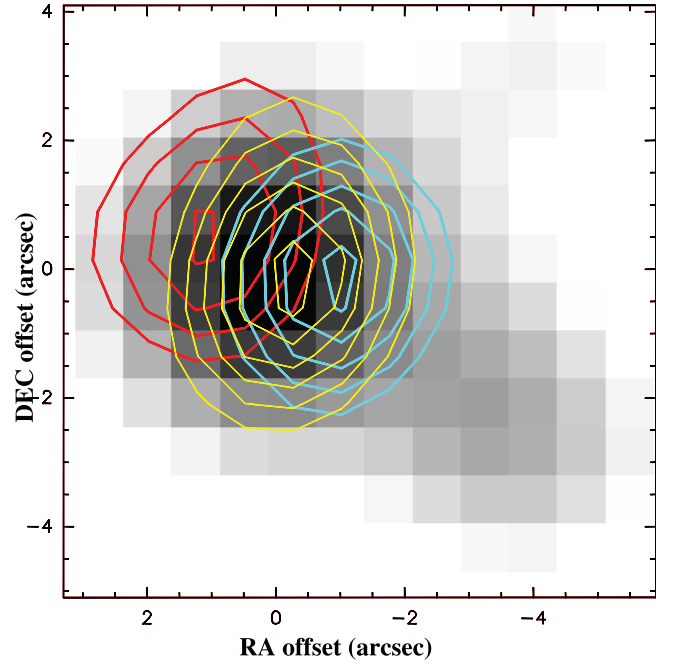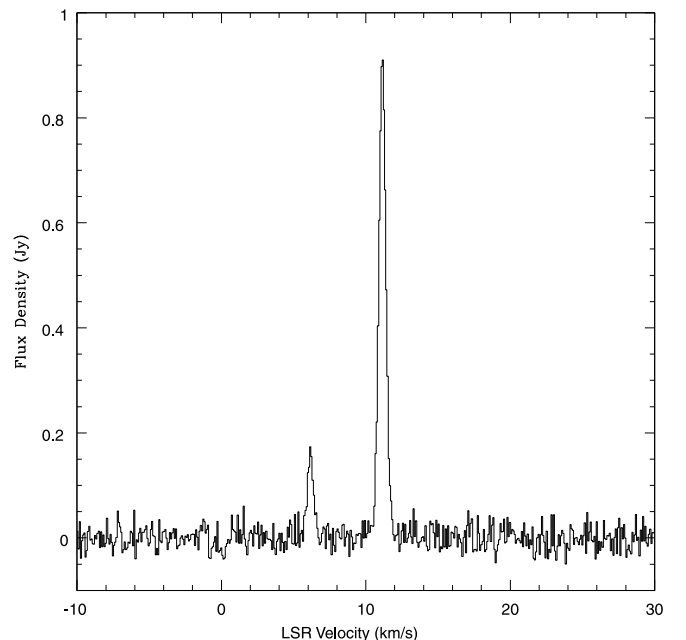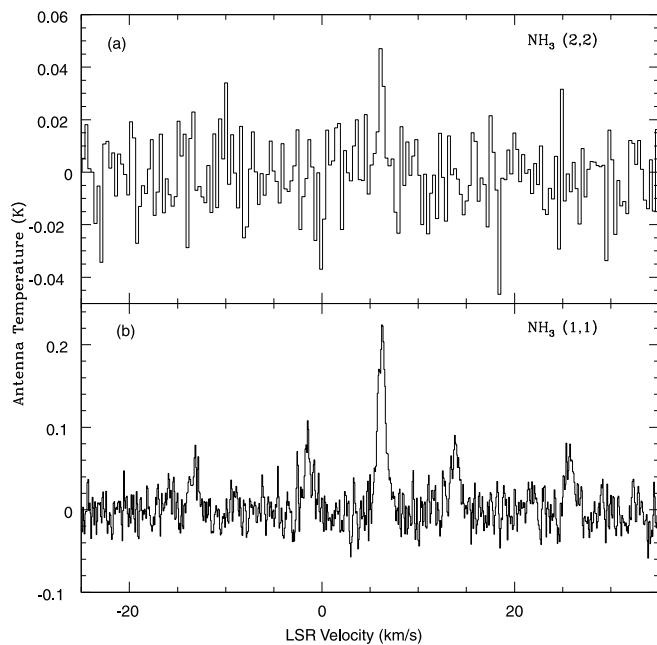FIG. 9.—Peak H$_2$O emission spectrum of IRAS 05506 observed with the GBT.

FIG. 10.—Ammonia emission observed with the GBT at the peak raster position. (a) The (2, 2) transition, boxcar-smoothed by a factor of 4 (to a resolution of 0.32 km s^{-1}), and resampled by the same factor. (b) The (1, 1) transition, without smoothing (resolution of 0.08 km s^{-1}).

and circular rotation. But given the Galactic longitude of $l_{II} = 185°$, and allowing a typical molecular cloud velocity dispersion of ~10 km s^{-1}, the possible distance range is not well constrained. In this paper we adopt a fiducial distance $D = 2.8$ kpc, and scale all of our estimates with D. At this distance, the bolometric luminosity of IRAS 05506 derived from integrating over its (very red) SED is $L \sim 5100$ $L_\odot$. The integration spans the full range of wavelengths covered by ISO archival spectra of this object, i.e., 2.4–198 μm. The uncertainty in estimating L due to flux beyond the wavelength limits of the SED is <5%.

Given the spectral type (late G to early K; i.e., $T_{\rm eff} \sim 5000$–4400 K) of the central star inferred from our optical spectroscopy, and the above luminosity, we can locate IRAS 05506 on the H-R diagram and compare with evolutionary models. Inspection of the pre-main-sequence stellar evolutionary models of Bernasconi & Maeder (1996) shows that the above values of $T_{\rm eff}$ and L lie between the tracks for stars with main-sequence masses of 9 and 15 $M_\odot$, and at the low-temperature end of these tracks—thus, close to the epoch where deuterium burning is initiated.

4.1. The Optical Knot Spray: Interstellar Bullets

We propose that the knots are Herbig-Haro objects based on their forbidden-line emission; they are seen most prominently in the F606W image compared to the images at longer wavelengths because this filter covers the Hα and [N II] lines. The [S II] $\lambda6716/\lambda6731$ ratio, $R_{\rm [S\,II]}$, is about 0.6 (0.5) for the low- (high-) velocity emission in the knots, implying electron densities of about 3300 (8000) cm^{-3} assuming an electron temperature of 10^4 K (Canto et al. 1980). Using the average value of $R_{\rm [S\,II]}$ for knot K1 (0.54), we derive $n_e = 6000$ cm^{-3}, and approximating K1's shape with a prolate ellipsoid having major (minor) axis = 0.29″ (0.15″), we find, assuming $n_e = n_{\rm H}$, that its mass is $M_{\rm K1} = 2 \times 10^{-5}$ $(D/2.8$ kpc$)^3$ $M_\odot$. The knots K2–K4 are somewhat fainter (by factors of 2–3) than K1, and therefore may have correspondingly lower, but comparable, masses.

The morphology and kinematics of the fanlike spray of elongated knots in IRAS 05506 are similar to the interstellar bullets seen in H$_2$ (2.12μm) and [Fe II] (1.65μm) emission toward the Orion molecular cloud (e.g., Allen & Burton 1993). Allen & Burton (1993) derive a minimum mass of $\sim10^{-5} M_\odot$ for the Orion bullets, comparable to our value for knot K1. The opening angle of the bullet spray in IRAS 05506 is about 45° (70°), measured from knot K8 to k10 (k12), and hence is somewhat smaller than the almost 90° opening angle covered by the Peak 1 region (located northwest of the BN object and Source I) shown in Nissen et al. (2007). The Orion bullets are typically 2″–4″ in angular extent (Tedds et al. 1999); if we assume that the physical size of the IRAS 05506 bullets is similar, then their smaller angular sizes suggest that IRAS 05506 is about a factor of 10 more distant than Orion, i.e., at 4.5 kpc. The total (angular) radial extent covered by the bullets in the Peak 1 Orion region is about 35″–40″, i.e., a factor of 6–7 times larger than that measured for the IRAS 05506 bullets region—consistent with a larger distance to the latter by a similar factor, if we assume similar physical extents for the bullet regions of these two sources. The 6–10 times larger distance to IRAS 05506 could also account naturally for the fact that the number of high-velocity knots in IRAS 05506 is much smaller than that found toward Orion, since we presumably detect only the most extreme (i.e., brightest and largest) members of a larger collection of knots. Similarly, it may be that the opening angle of the IRAS 05506 bullet region is intrinsically comparable to that found for Orion, but our current observations lack the sensitivity needed to detect lower brightness knots at wider opening angles because of IRAS 05506's much larger distance. Furthermore, if the filamentary structures seen in the F110W image (Fig. 2), together with knots k13 and k14, represent the unresolved or partially resolved counterpart to the bullet spray seen to the east of Sa, then the similarity to the Orion bullet spray becomes even more pronounced.

For knot K1, which is the most distant knot from Sa, we estimate an expansion timescale of 200 ($D/2.8$ kpc) yr, under the assumption that the FWZI of the velocity profile of a bow shock is equal to the intrinsic speed of the bullet producing the bow shock (Hartigan et al. 1987). For knot K2, which is closer to Sa than K1, the expansion speed, inferred as above, is smaller (~300 km s^{-1}), and we find an expansion timescale of about 170 ($D/2.8$ kpc) yr. We do not know if all the knots were ejected quasi-simultaneously over some modest range of velocities from the central source, or result from an episodic outflow which ejects high-speed blobs intermittently over a wide range of position angles.

In addition, we have examined the literature on a few other examples of possibly similar systems with high-velocity knots. For example, the high-mass YSO IRAS 18151−1208 contains knots spread along two roughly orthogonal axes, and they are related to two well-defined collimated outflows (Davis et al. 2004). The outflows HH 212 and HH 211, which arise from low-mass protostars, also have very highly collimated outflows (Lee et al. 2006, 2007). Thus, these three YSOs are morphologically quite dissimilar to the knotty ejections from IRAS 05506, which have an opening angle of at least 44°. The high-mass YSO IRAS 05358+3843 displays a fan of knots seen in near-IR H$_2$ emission, and for this source Kumar et al. (2002) make a similar analogy to the Orion bullets.

The optical jet, Sa-jet, is much bluer than the central source, Sa-pk, presumably because, like the knots, it is dominated by optical line emission. The rather precise alignment of the position angle of this jet, which is seen out to a radius of 0.25″ from Sa-pk,

to that of the more extended high-velocity outflow seen in our millimeter-wave interferometric data, is remarkable. Is this outflow different in nature from that which produced the bright knots K1–K4, since no such knots appear to be associated with it? It may be that such knots are present, but not visible due to local extinction. The average large-scale (i.e., over a 0.5′ area) extinction derived from our NH_3 data (see § 4.2 below) is $A_V \sim 3$, and it is likely that the extinction increases steeply toward Sa. Indeed, we find that the line-of-sight extinction to Sa is $A_V \sim 25$ by comparing each of our observed 1.6 and 2.2 μm fluxes of the central star with the values expected based on its bolometric flux and effective temperature. We have used the tabulated average extinction curve in Whittet (1992) to derive the visual extinction from our near-IR values. A faint patch of nebulosity is seen in the F606W image at an offset of about 3.5″ along the P.A. of the optical jet, but it does not have a well-delineated structure like the K1–K4 knots and is similar to other faint diffuse nebulosities seen in the vicinity of Sa, so it is not clear whether or not it is directly associated with the jet.

4.2. The Gas and Dust Environment

The physical properties of the molecular gas associated with, and/or in the vicinity of IRAS 05506 on an arcminute angular scale can be inferred from the ammonia data. Using Gaussian fits to the ammonia line profiles to estimate the peak intensities, and the formalism given by Wilson et al. (1993) and Ungerechts et al. (1986), we estimate the opacity of the (1,1) transition ($\tau \sim 0.7$ for the main line) and the rotational temperature between the (2,2) and (1,1) transitions ($T_{rot} = 12.5 \pm 2.2$ K). The rotational temperature is a lower limit to the kinetic temperature, T_{kin}; for these low values of T_{rot}, $T_{kin} \approx T_{rot}$ (Morris et al. 1973; Danby et al. 1988). Assuming a beam filling factor of unity, the ammonia column density toward the peak of the emission is $N_{NH_3} \sim 1.1 \times 10^{14}$ cm^{-2}. Estimating the region of ammonia emission to have a diameter of 1′, and adopting a fractional NH_3/H_2 abundance ratio (by number),[12] $f(NH_3) = 4 \times 10^{-8}$, we obtain a molecular hydrogen mass in this region of 11 $(D/2.8$ kpc$)^2$ $M_\odot$. In this calculation, we have accounted for the lower emission at the outer regions of the source by assuming that the derived mass is a factor of 2 lower than the value that would result from assuming uniform emission within the 1′ region. We estimate that the large-scale visual extinction toward the center of the cloud is, $A_V \sim 3$, using a ratio $N(H_2)/A_V = 0.94 \times 10^{21}$ cm^{-2} mag^{-1} (Frerking et al. 1982).

The virial mass of the cloud (assuming an r^{-1} density distribution) is $M_{vir} = 188$ $(R/pc)(\Delta V_{1/2}/km$ s$^{-1})^2 = 73$ $(D/2.8$ kpc$)$ $(\theta/0.5′)$ $M_\odot$, where θ is the cloud radius in angular units, and $\Delta V_{1/2} = 0.96$ km s^{-1}. For an r^{-2} density cloud, we get $M_{vir} = 48$ $(D/2.8$ kpc$)(\theta/0.5′)$ $M_\odot$. The factor of 4 (or more) discrepancy between the virial cloud mass and that derived from the ammonia data may easily be attributed to the large uncertainties in our assumed value of $f(NH_3)$ and source distance, and/or to nongravitational linewidths, such as unresolved outflow motion.

We have very recently (2007 November) mapped the ^{12}CO $J = 1–0$ emission in a $36′ \times 18′$ ($\Delta\alpha \times \Delta\delta$) region around IRAS 05506 using the ARO 12 m millimeter-wave telescope, and find the presence of a molecular cloud which extends over at least 30′ east-west and 12′ north-south. Observations of the ^{13}CO and C ^{18}O $J = 1–0$ emission toward the central region show that the ^{12}CO line is optically thick, both in the line core and wings. We will discuss these data in detail in a future publication; our
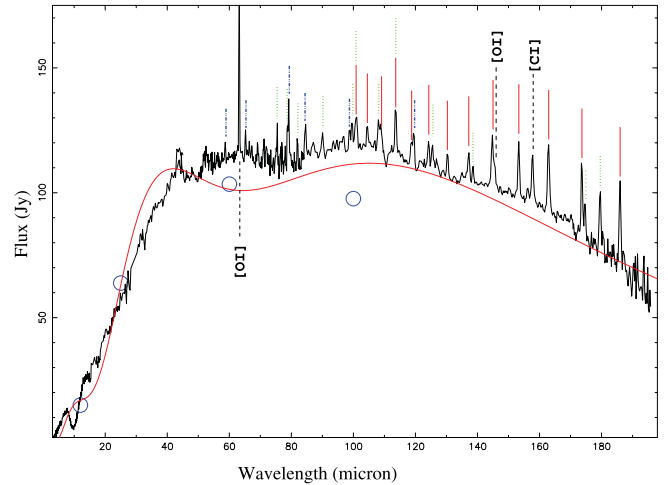
---

[12] Pillai et al. (2006) find values in the range $(0.7–10) \times 10^{-8}$.

Fig. 11.—*ISO* SWS and LWS spectra of IRAS 05506, showing a deep 10 μm amorphous silicate absorption feature, and emission in the O I (at 63 and 146 μm; *dashed vertical bars*) and C II (158 μm: *dashed vertical bar*) lines, as well as numerous far-infrared CO, OH, and H_2O lines. The locations of the CO lines from $J = 14–13$ (186.0 μm) to $J = 26–25$ (100.5 μm) are shown by short solid vertical red bars, and those of the most prominent lines of H_2O (both ortho and para) and OH are marked by green dotted and blue double-dot-dashed vertical bars, respectively. The symbols show broadband photometric data from *IRAS*. The red curve shows a simple dust model fitted to the data.

---

preliminary analysis shows that the extended cloud which we detect in ^{12}CO $J = 1–0$ emission is easily many hundreds of solar masses.

The molecular cloud detected in NH_3 emission is presumably associated with the extended diffuse nebulosity which is seen in the 2MASS images. The nebulosity is most likely due to scattered light from dust. In order to estimate the dust mass associated with this cloud, we have retrieved and recalibrated archival *ISO* SWS and LWS spectra of IRAS 05506 covering the 3–200 μm wavelength range (Fig. 11). We find that it shows a very red continuum, a deep 10 μm amorphous silicate absorption feature, and emission in numerous far-infrared CO, OH, and H_2O lines, as well as the O I (at 63 and 146 μm) and C II (158 μm) lines (R. Sahai & G. Sarkar 2008, in preparation). The far-IR line spectrum of IRAS 05506 is very similar to that seen toward the low-mass protostar IRAS 16293−2422 (Ceccarelli et al. 1998). A multicomponent dust model (i.e., with "cool," "warm," and "hot" components; Sahai et al. 1991) assuming a power-law (λ^{-p}, with $p = 1.5$) dust emissivity with a value of 150 cm^2 g^{-1} (per unit *dust* mass) at 60 μm (Jura 1986) provides a modest fit to the SED, and demonstrates that the bulk of the mass is in cool dust. We find that the cool component has 0.26 $M_\odot$ of dust at 27 K, and the warm component has 0.22×10^{-2} $M_\odot$ of dust at 79 K; both masses scale as $(D/2.8$ kpc$)^2$. These imply a total mass of 26 $M_\odot$ (assuming a gas-to-dust ratio, $g_d = 100$), which compares reasonably well with that derived from our ammonia observations. Note that the above modeling can provide only a rough estimate of the mass because the dust is expected to be distributed over a range of temperatures, depending on the distance from the heating source(s). Sahai et al. (2007) have compared the results of such modeling with those from more accurate modeling (using a dust radiative transfer code) for PPNs, and find that the simple modeling gives dust masses that are lower by factors of 0.6–0.8.

For the millimeter-continuum source associated with Sa, we derive a dust mass of 0.011–0.032 $(D/2.8$ kpc$)^2$ $M_\odot$, assuming 79–27 K for the temperature of the dust, and that $p = 1.5$ is valid over the $\lambda = 60$ μm to 2.6 mm wavelength range. Thus, the total

mass associated with Sa within a $\sim 4''$ size region is $1.1–3.2\ M_\odot$ (assuming g_d as above). The total molecular mass derived from the CO flux detected with the OVRO beam, i.e., within a $\sim 3.4''$ size region, is $0.26\ M_\odot$ assuming a fractional CO/H$_2$ abundance ratio, $f(CO) = 10^{-4}$, and taking $T_{rot} = 27$ K.[13] Because the CO is optically thick, this value represents a lower limit.

The inadequacies of the SED fit from our simple model indicate that the source has dust over a wide range of temperatures. R. Sahai & G. Sarkar (2008, in preparation) have therefore used the online tool provided by Robitaille et al. (2007), which provides least-squares fits of precomputed disk-envelope models of YSOs to user-defined SEDs, in order to fit IRAS 05506's SED. Given an input distance range of 0.1–5 kpc, the fitting tool finds that the first three best-fit models to the SED of IRAS 05506 have, respectively, distances of $D = 2.2$, 2.6, and 3.0 kpc (implying bolometric luminosities in the range 3150–5850 $L_\odot$), central star masses of $M = 8.5$, 10.6, and 11.2 $M_\odot$, and $T_{eff} = 4190$, 4430, and 4280 K. These T_{eff} values are consistent with the spectral type of the central star inferred from our optical spectroscopy.

4.3. Molecular Outflow: Mass and Dynamics

We estimate the mass (M_{bip}), mass-outflow rate ($\dot{M}_{bip}$), scalar momentum (P_{sc}), mechanical energy (E_{mech}), and mechanical power (L_{mech}) in the high-velocity bipolar outflow using the integrated CO $J = 1–0$ line profile from our OVRO data. The derived values for M_{bip}, P_{sc}, and E_{mech} scale as $(D/2.8\ \text{kpc})^2$, whereas $\dot{M}_{bip}$ and L_{mech} scale as $D/2.8$ kpc. The scalar momentum and the mechanical energy are computed using the methodology described in Bujarrabal et al. (2001). As before, we assume $T_{rot} = 27$ K, $f(CO) = 10^{-4}$, and the emission to be optically thin—since the CO emission is optically thick, our derived values are lower limits. In this analysis, we use the $J = 1–0$ emission flux over the V_{LSR} velocity ranges [10.4, 119.6] km s^{-1} for the red component and [2.6, −106.6] km s^{-1} for the blue component of the outflow shown in Figure 8. We have conservatively excluded emission in the central three 1 MHz channels which cover the line core. We infer an expansion timescale for the outflow of 185 yr, by dividing the linear separation between the red and blue outflow components by the mean separation velocity, 156 km s^{-1} (derived from the difference between the average velocities for the red and blue components in Fig. 8) and assuming an intermediate inclination (45°) of the outflow axis relative to the line of sight. We find $M_{bip} > 0.18\ M_\odot$, $\dot{M}_{bip} > 9.7 \times 10^{-4}\ M_\odot\ \text{yr}^{-1}$, and $P_{sc} > 8.6 \times 10^{38}$ g cm s^{-1} (4.3 $M_\odot$ km s^{-1}). The mechanical energy in the bipolar outflow is $E_{mech} > 4.6 \times 10^{45}$ erg; dividing this by the expansion timescale, we obtain $L_{mech} > 7.9 \times 10^{35}$ erg s^{-1}. Hence, the ratio of the mechanical power to the stellar luminosity is $L_{mech}/L > 0.04$, which is significantly larger than the values typically found for YSO outflows (10^{-3} to 10^{-2}; Lada 1985). The outflow cannot be driven by radiation pressure: the expansion timescale, ~ 185 yr, is much smaller than the time required by radiation pressure to accelerate the observed bipolar outflow to its current speed, $t_{rad} = P_{sc}/(L/c) \sim 4 \times 10^4$ yr.

5. DISCUSSION

The morphology of IRAS 05506 does not resemble that of any known PPN. Although its luminosity (at a distance of 2.8 kpc) is commensurate with that expected for PPNs, the circumstellar mass is significantly larger than that typically found in PPNs

($\lesssim 1\ M_\odot$; e.g., Sahai et al. 2007). Zinchenko et al. (1998) include IRAS 05506 (labeled by its Galactic coordinates, as G184.96− 0.85) in their study of dense molecular cores in regions of massive star formation, and find CO $J = 1–0$, CS, and C^{34}S $J = 2–1$ emission toward this object using the Onsala 20 m telescope (beam sizes $35''$ and $40''$). The radial velocity of the CS line, 6.2 km s^{-1} V_{LSR}, agrees with that found from our NH$_3$ observations, so there can be little doubt that the CS emission is probing the same molecular cloud core as NH$_3$. Our recent mapping of CO $J = 1–0$ emission toward IRAS 05506 with the ARO 12 m dish shows the presence of a very extended molecular cloud with a total mass of at least several hundred solar masses.

IRAS 05506 is, in all likelihood, not a PPN. The 1612 MHz OH maser line profile in IRAS 05506, observed with the Arecibo dish (Chengalur et al. 1993), does not show the typical double-peaked shape seen toward most AGB stars or PPNs. The main lines of OH at 1665 and 1667 MHz were detected by Lewis (1997) at Arecibo; the emission covers about 15 km s^{-1} in the 1612 MHz line and $\sim 40–45$ km s^{-1} in the main lines. The combined presence of maser (H$_2$O and OH), NH$_3$, CO, CS, and C^{34}S, and relatively strong far-IR emission strongly argues for a dense, star-forming core being associated with IRAS 05506. Palagi et al. (1993) also classify IRAS 05506 as a star formation region, on the basis of a principal component analysis of the IRAS colors of all H$_2$O maser sources in the Arcetri Catalog (Comoretto et al. 1990) which had IRAS PSC counterparts. The very short expansion timescale of the optical knots and the fast molecular outflow indicates that the source Sa is a very young protostar.

The presence of OH maser emission argues for IRAS 05506 not being a low-mass YSO, since there are no known OH masers toward low-mass YSOs. There have been surveys for OH maser emission from, e.g., T Tauri stars (C. J. Chandler et al., private communication), but no detections have been made and we are unaware of any published detections of OH masers toward low-mass YSOs. Given our calculated luminosity at $D = 2.8$ kpc, our distance estimate would have to be lower by at least a factor of 4 for the luminosity to be in the range for low-mass YSOs.

Is IRAS 05506 an intermediate-mass or massive YSO? In a search of the literature on OH masers toward star-forming regions, we found only one region (L1287) which does not appear to be forming massive stars and which shows an OH maser (Wouterloot et al. 1993). This region contains the FU Ori–type objects RNO 1B and RNO 1C and an IRAS source (IRAS 00338+6312) whose luminosity indicates it to be an intermediate-mass YSO. So there is a small probability that IRAS 05506 is associated with an intermediate-mass star (Quanz et al. 2007 and references therein). Furthermore, the total molecular cloud mass derived from the ammonia data is rather small for a massive star, because the implied efficiency of star formation would have to be significantly higher than is usually assumed to be the case. Note, however, that this issue is a lesser concern if the source were at a distance exceeding 5 kpc, because of the scaling of the cloud mass with the square of the distance. Also, the extended molecular cloud toward IRAS 05506 seen via CO mapping harbors several hundreds of solar mass of material (for $D = 2.8$ kpc) within a region 3 times bigger in size than that probed by our ammonia data. Although CO masses are not the best measure of the mass of a cloud core, the total mass of the associated cloud is likely well above what is needed to support massive star formation. It is perhaps unwarranted to be too concerned about the relatively low value of the cloud core mass, given the possibility that the core has been strongly altered or dissipated in the star formation process, especially in the presence of the observed strong outflows.

[13] If the excitation temperature is higher, the derived mass will be larger; e.g., for $T_{rot} = 79$ K, the derived mass is a factor of 2.5 larger.

The multiple optical knots in IRAS 05506 imply that material has been ejected from the central source in the form of high-speed bullets rather than in a continuous fashion. The presence of this wide-angle spray of bullets in IRAS 05506 indicates, by analogy with Orion, that the launching source may be a massive proto-star. A massive star, depending on its evolutionary status, could produce an ultracompact H II region with detectable continuum emission. But since we do not find a measurable radio continuum toward IRAS 05506, either it is not a massive star, or (1) the central H II region is still very small, (2) the source is sufficiently distant that its radio continuum is below our noise limit, (3) the central star has been caught at a very early age while its temperature is still too low to provide sufficient UV flux for ionization—this possibility is consistent with the late spectral type of the central star inferred from our optical spectroscopy.

We compare IRAS 05506 with the high-mass protostellar objects (HMPOs) identified by Sridharan et al. (2002, hereafter S02). These HMPOs are dense molecular cores detected in a CS $J = 2$–1 survey of massive star-forming regions, which are bright at FIR wavelengths ($F60 > 90$ Jy) and generally have low (or absent) centimeter radio fluxes. IRAS 05506 satisfies these selection criteria for HMPOs, but shows a significantly smaller NH_3 line width ($\Delta V_{NH_3} = 0.96$ km s^{-1}) and kinetic temperature (12.5 K) than the median values for HMPOs ($\Delta V_{NH_3} = 1.9$ km s^{-1} and $T_{kin} = 18.5$ K: derived, as for IRAS 05506, from single-dish ammonia observations). In fact, T_{kin} for IRAS 05506 is lower than the smallest value for the 40 HMPOs in which T_{kin} was measured.

S02 made two-component dust model fits to the *IRAS* fluxes for these HMPOs and find cold dust components with $T_d \sim$ 30–70 K, and hot components with $T_d \sim$ 100–250 K; i.e., somewhat higher than the corresponding ones for IRAS 05506. The bulk of the luminosity for the HMPOs comes from the cool component, as we have found for IRAS 05506. The luminosity of IRAS 05506 is comparable to those found for many objects in the HMPO list of S02. However, the associated IRAS fluxes (at 60 μm; only upper limits to the 100 μm fluxes are available for most HMPOs) and thus the derived masses of the cool dust component for HMPOs with comparable (near) kinematic distances are generally higher than that for IRAS 05506, by factors of $\sim$1.5 or more.

IRAS 05506's ammonia line width and gas kinetic temperature are even lower than the median values (1.5 km s^{-1} and 16.9 K) for high-mass starless cores (HMSCs: Sridharan et al. 2005), which are apparently less evolved than HMPOs. HMPOs, but not HMSCs, have *MSX* Point Source Catalog counterparts, indicative of the presence of a luminous, hot, central source. IRAS 05506 may thus be an extreme example of the HMPO class, lying at the bottom end of the ammonia line width and kinetic temperature distributions (see, e.g., Fig. 3 of Sridharan et al. 2005), and thus at the lower end of the mass range for these objects. In a plot of HMPO core mass (derived from single-dish millimeter-continuum data) versus FIR luminosities (Fig. 6 of S02), there are two sources with core masses comparable to that derived from the millimeter continuum for IRAS 05506. Given that the latter is based on interferometric observations, which resolve out flux on scales more extended than about 4″, whereas the core masses in S02's Figure 6 are based on single-dish (beam size 11″) observations, IRAS 05506's millimeter-continuum core mass likely compares well with even higher core-mass sources in S02's Figure 6, which has three more sources with core masses less than about 30 $M_\odot$. We note that the HMPO list of S02 may well include stars at the upper end of the intermediate-mass range (i.e., 8 $M_\odot$); for example, we have found at least one example of an HMPO from

this list, IRAS 20126+4104, for which recent observations suggest a mass of about 7 $M_\odot$ (Cesaroni et al. 2005).

The optical detection of IRAS 05506 might seem surprising, considering the general lack of optical detections of HMPOs. It is plausible that the outflows from IRAS 05506 have cleared away enough circumstellar cloud material from the near vicinity of the central star, allowing a detectable amount of starlight at optical wavelengths to leak out and be scattered into our line of sight by dust in the walls of the cavity cleared out by the outflow. Note that this scenario does not require the outflow cavity to be directed exactly along the line of sight. In addition, we do not know the inclination and opening angles of the molecular outflow, and it is quite possible that these are sufficiently favorable for the above scenario to be feasible.

The jetlike feature emanating from the central source is directed along an axis roughly orthogonal to the average position angle for the most prominent knots. This suggests that either the collimated outflow which created the knots has suffered a drastic change in direction, or Sa-jet is the result of an independent high-velocity outflow. If the latter hypothesis is correct, it could indicate the presence of an unresolved binary star associated with source Sa. Taking the lowest value (3150 $L_\odot$) of the total luminosity as derived from the SED modeling (§ 4.2), and dividing it equally between the two stars in the binary, we find that these stars lie on the Bernasconi & Maeder (1996) pre-main-sequence tracks for 9 $M_\odot$ stars. Hence, even if the central star is a binary, at least one of the components is a massive star (i.e., if D is 2.2 kpc or larger). Note that the expansion timescales derived for the fast molecular outflow and the fast-moving optical knots are very similar, indicating that these were initiated quasi-simultaneously in IRAS 05506's recent history. So if the optical and molecular outflows are produced from different stars in a binary system, their similar expansion timescales suggest a common triggering mechanism for launching them.

6. CONCLUSIONS

We have made a serendipitous discovery of an enigmatic outflow source, IRAS 05506+2414, as part of a multiwavelength survey of pre-planetary nebulae. Subsequent to the *HST* imaging, we carried out optical spectroscopy, millimeter-wave interferometry of the CO $J = 1$–0 line, and water and methanol maser line and ammonia inversion line observations at $\sim$22–25 GHz.

1. The *HST* optical and near-infrared images show a bright compact central source, and a fanlike spray of high-velocity (projected radial velocity 350 km s^{-1}) elongated knots which appear to emanate from it. These structures appear to be analogous to the near-IR "bullets" around the Orion KL Nebula and to have similar masses ($\sim 10^{-5}$ $M_\odot$). The central source shows a jetlike extension along P.A. $\sim 230°$, which is roughly orthogonal to the average direction of the bullet spray seen in the optical images.

2. The high-resolution (3.9″ × 2.9″) CO $J = 1$–0 data show a compact emission core of size ($\lesssim 5″$); the line profile has a narrow core and weak, high-velocity wings. The latter represent emission from a high-velocity bipolar outflow directed along the optical jet feature. A 10 mJy continuum source (at $\lambda = 2.6$ mm) is also seen at the same location as the line peak. The continuum source structure consists of an unresolved core and a possible faint extension whose orientation is consistent with the optical jet and high-velocity molecular outflow direction.

3. H_2O maser emission was detected both with the VLA and the GBT. With the latter, NH_3 (1,1) and (2,2) lines were detected, but no methanol emission was found (rms antenna temperature

was ∼25 mK). The H$_2$O maser emission is spatially unresolved. Our map of NH$_3$ emission shows an extended molecular cloud of size about 1′, with a kinetic temperature of 12.5 K and a mass of about 11 $M_\odot$, assuming a fractional NH$_3$/H$_2$ abundance ratio (by number), $f(NH_3) = 4 \times 10^{-8}$, and a distance of 2.8 kpc. In comparison, the virial mass of the cloud is 48(73) $M_\odot$, for an r^{-2} (r^{-1}) density distribution. The factor of 4 (or more) discrepancy between the virial cloud mass and that derived from the ammonia data may be attributed to the large uncertainty in our assumed value of $f(NH_3)$ and the distance, and/or to non-gravitational linewidths, such as unresolved outflow motion.

4. The 8 GHz continuum observations show no continuum emission (3 σ upper limit of 150 μJy) within a field of approximately 40″ diameter centered on the position of IRAS 05506.

5. IRAS 05506 is most likely not a PPN. The combined presence of H$_2$O and OH maser, far-IR, NH$_3$, CO, CS, and C^{34}S emission strongly argues for a dense, star-forming core being associated with IRAS 05506. IRAS 05506 is most likely either a massive or intermediate-mass YSO, but not a low-mass YSO. If it is a massive star then the lack of radio continuum and the late G to early K spectral type we find for the central star implies that in IRAS 05506 we are witnessing the earliest stages of a massive star's life, while its temperature is still too low to provide sufficient UV flux for ionization.

6. IRAS 05506 resembles objects in a recently identified class of high-mass protostellar objects (HMPOs). Given the relatively low gas kinetic temperature and narrow line width derived from the ammonia data, IRAS 05506 could be an extreme member of this class, lying at the lower end of the mass range for these objects.

7. A multicomponent dust model provides a reasonable fit to the mid- to far-infrared SED of IRAS 05506; we find that the bulk of the mass is in a cool dust component with a temperature of 27 K and a total (gas+dust) mass of 26 $M_\odot$ (and about 1% of this in a warmer component at 79 K), assuming a gas-to-dust ratio of 100. The 2.6 mm continuum flux measured with OVRO gives a total mass of 1.1–3.2 $M_\odot$ in a ∼4″-size region around source Sa, assuming dust temperatures in the range 79–27 K.

8. Both the molecular high-velocity outflow and that producing the optical knots have extremely short and similar expansion timescales of about 200 yr, suggesting that either these are manifestations of a common ejection event in IRAS 05506's recent past, or if they are due to independent ejections, there must have been a common triggering mechanism for launching them. The molecular outflow cannot be driven by radiation pressure, since the expansion timescale is orders of magnitude smaller than the time required by radiation pressure to accelerate the observed bipolar outflow to its current speed.

9. We have estimated the physical parameters of the high-velocity bipolar outflow from the interferometric CO data— our estimates are lower limits because the CO emission is optically thick. We find that the outflow mass is $M_{bip} > 0.18\ M_\odot$, the mass-outflow rate is $\dot{M}_{bip} > 9.7 \times 10^{-4}\ M_\odot\ yr^{-1}$, the scalar momentum is $P_{sc} > 4.3\ M_\odot\ km\ s^{-1}$, the mechanical energy is $E_{mech} > 4.6 \times 10^{45}$ erg, and the mechanical power is $L_{mech} > 7.9 \times 10^{35}$ erg s^{-1}.

REFERENCES

Allen, D. A., & Burton, M. G. 1993, Nature, 363, 54
Bernasconi, P. A., & Maeder, A. 1996, A&A, 307, 829
Bujarrabal, V., Castro-Carrizo, A., Alcolea, J., & Sánchez Contreras, C. 2001, A&A, 377, 868
Canto, J., Meaburn, J., Theokas, A. C., & Elliott, K. H. 1980, MNRAS, 193, 911
Ceccarelli, C., et al. 1998, A&A, 331, 372
Cesaroni, R., Neri, R., Olmi, L., Testi, L., Walmsley, C. M., & Hofner, P. 2005, A&A, 434, 1039
Chengalur, J. N., Lewis, B. M., Eder, J., & Terzian, Y. 1993, ApJS, 89, 189
Comoretto, G., et al. 1990, A&AS, 84, 179
Condon, J. J., Cotton, W. D., Greisen, E. W., Yin, Q. F., Perley, R. A., Taylor, G. B., & Broderick, J. J. 1998, AJ, 115, 1693
Cutri, R. M., et al. 2003, The IRSA 2MASS All-Sky Point Source Catalog (Pasadena: Caltech), http://irsa.ipac.caltech.edu/applications/Gator/
Danby, G., Flower, D. R., Valiron, P., Schilke, P., & Walmsley, C. M. 1988, MNRAS, 235, 229
Davis, C. J., Varricatt, W. P., Todd, S. P., & Ramsay Howat, S. K. 2004, A&A, 425, 981
Frerking, M. A., Langer, W. D., & Wilson, R. W. 1982, ApJ, 262, 590
Egan, M. P., et al. 1999, US Air Force Res. Lab. Tech. Rep. AFRL-VS-TR-1999-1522 (Wright-Patterson AFB: Air Force Res. Lab.)
Goodrich, R. W. 1991, ApJ, 376, 654
Hartigan, P., Raymond, J., & Hartmann, L. 1987, ApJ, 316, 323
Jura, M. 1986, ApJ, 303, 327
Kumar, M. S. N., Bachiller, R., & Davis, C. J. 2002, ApJ, 576, 313
Lada, C. J. 1985, ARA&A, 23, 267
Lee, C.-F., Ho, P. T. P., Beuther, H., Bourke, T. L., Zhang, Q., Hirano, N., & Shang, H. 2006, ApJ, 639, 292
Lee, C.-F., Ho, P. T. P., Palau, A., Hirano, N., Bourke, T. L., Shang, H., & Zhang, Q. 2007, ApJ, 670, 1188

Lewis, B. M. 1997, ApJS, 109, 489
Manchado, A., Garcia-Lario, P., Sahu, K., & Pottasch, S. R. 1990, A&AS, 84, 517
Morris, M., Zuckerman, B., Palmer, P., & Turner, B. E. 1973, ApJ, 186, 501
Nissen, H. D., Gustafsson, M., Lemaire, J. L., Clénet, Y., Rouan, D., & Field, D. 2007, A&A, 466, 949
Palagi, F., Cesaroni, R., Comoretto, G., Felli, M., & Natale, V. 1993, A&AS, 101, 153
Pillai, T., Wyrowski, F., Carey, S. J., & Menten, K. M. 2006, A&A, 450, 569
Quanz, S. P., Henning, T., Bouwman, J., & Linz, H. 2007, ApJ, 658, 487
Robitaille, T. P., Whitney, B. A., Indebetouw, R., & Wood, K. 2007, ApJS, 169, 328
Sahai, R., Morris, M., Sánchez Contreras, C., & Claussen, M. J. 2007, AJ, 134, 2200
Sahai, R., Sánchez Contreras, C., & Morris, M. 2005, ApJ, 620, 948
Sahai, R., Wooten, A., Schwarz, H. E., & Clegg, R. E. S. 1991, A&A, 251, 560
Sánchez Contreras, C., Sahai, R., Gil de Paz, A., & Goodrich, R. 2008, ApJ, submitted
Sheinis, A. I., Bolte, M., Epps, H. W., Kibrick, R. I., Miller, J. S., Radovan, M. V., Bigelow, B. C., & Sutin, B. M. 2002, PASP, 114, 851
Sridharan, T. K., Beuther, H., Saito, M., Wyrowski, F., & Schilke, P. 2005, ApJ, 634, L57
Sridharan, T. K., Beuther, H., Schilke, P., Menten, K. M., & Wyrowski, F. 2002, ApJ, 566, 931 (S02)
Tedds, J. A., Brand, P. W. J. L., & Burton, M. G. 1999, MNRAS, 307, 337
Ungerechts, H., Winnewisser, G., & Walmsley, C. M. 1986, A&A, 157, 207
Whittet, D. C. B. 1992, Dust in the Galactic Environment (Bristol: IOP), 67
Wilson, T. L., Gaume, R. A., & Johnston, K. J. 1993, ApJ, 402, 230
Wouterloot, J. G. A., Brand, J., & Fiegle, K. 1993, A&AS, 98, 589
Zinchenko, I., Pirogov, L., & Toriseva, M. 1998, A&AS, 133, 337